





RESEARCH ARTICLE | JANUARY 20 2022

Spintronic emitters for super-resolution in THz-spectral imaging

Special Collection: [Ultrafast and Terahertz Spintronics](#)

Finn-Frederik Stiewe; Tristan Winkel ; Yuta Sasaki; Tobias Tubandt; Tobias Kleinke; Christian Denker; Ulrike Martens; Nina Meyer ; Tahereh Sadat Parvini; Shigemi Mizukami ; Jakob Walowski ; Markus Münzenberg

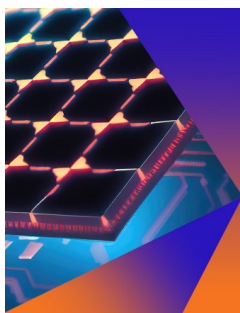


Appl. Phys. Lett. 120, 032406 (2022)

<https://doi.org/10.1063/5.0076880>



CrossMark



Applied Physics Letters

Special Topic:
Hybrid and Heterogeneous Integration in Photonics:
From Physics to Device Applications

Submit Today



Spintronic emitters for super-resolution in THz-spectral imaging

Cite as: Appl. Phys. Lett. **120**, 032406 (2022); doi: [10.1063/5.0076880](https://doi.org/10.1063/5.0076880)

Submitted: 28 October 2021 · Accepted: 5 January 2022 ·

Published Online: 20 January 2022







View Online



Export Citation



CrossMark

Finn-Frederik Stiewe,¹ Tristan Winkel,¹  Yuta Sasaki,^{2,3} Tobias Tubandt,¹ Tobias Kleinke,¹ Christian Denker,¹ Ulrike Martens,¹ Nina Meyer,¹  Tahereh Sadat Parvini,¹ Shigemi Mizukami,^{3,4,5}  Jakob Walowski,^{1,a)}  and Markus Münzenberg¹

AFFILIATIONS

¹Institut für Physik, Universität Greifswald, Greifswald, Germany

²Department of Applied Physics, Graduate School of Engineering, Tohoku University, Sendai, Japan

³WPI Advanced Institute for Materials Research (AIMR), Tohoku University, Sendai, Japan

⁴Center for Spintronic Research Network (CSRN), Tohoku University, Sendai, Japan

⁵Center for Science and Innovation in Spintronics (CSIS), Tohoku University, Sendai, Japan

Note: This paper is part of the APL Special Collection on Ultrafast and Terahertz Spintronics.

^{a)}Author to whom correspondence should be addressed: jakob.walowski@uni-greifswald.de

ABSTRACT

We investigate local THz field generation using spintronic THz emitters to enhance the resolution for micrometer-sized imaging. Far-field imaging with wavelengths above 100 μm limits the resolution to this order of magnitude. By using optical laser pulses as a pump, THz field generation can be confined to the area of laser beam focusing. The divergence of the generated THz beam due to laser beam focusing requires the imaged object to be close to the generation spot at a distance below the THz field wavelength. We generate THz-radiation by fs-laser pulses in CoFeB/Pt heterostructures, based on spin currents, and detect them by commercial low-temperature grown-GaAs (LT-GaAs) Auston switches. The spatial resolution of THz radiation is determined by applying a 2D scanning technique with motorized stages allowing step sizes in the sub-micrometer range. Within the near-field limit, we achieve spatial resolution in the dimensions of the laser spot size on the micrometer scale. For this purpose, a gold test pattern is evaporated on the spintronic emitter separated by a 300 nm SiO₂ spacer layer. Moving these structures with respect to the femtosecond laser spot, which generates THz radiation, allows for resolution determination. The knife-edge method yields a full-width half-maximum beam diameter of $4.9 \pm 0.4 \mu\text{m}$ at 1 THz. The possibility to deposit spintronic emitter heterostructures on simple glass substrates makes them attractive candidates for near-field imaging in many imaging applications.

© 2022 Author(s). All article content, except where otherwise noted, is licensed under a Creative Commons Attribution (CC BY) license (<http://creativecommons.org/licenses/by/4.0/>). <https://doi.org/10.1063/5.0076880>

Terahertz (0.6–10 THz) radiation provides great potential for biomedical applications, such as biosensing for cancer cell imaging, due to low non-ionizing photon energies and, thus, a non-destructive interaction of THz radiation with tissue.^{1–4} In addition, THz spectroscopy determines specific spectral fingerprints for numerous materials, which are not interfering with other spectral ranges, and, especially, water-based materials show strong absorption.^{5,6} This imaging technique is already used in airports to distinguish macroscopically sized materials from human cell tissue. Increasing the imaging resolution to the micrometer scale will provide new insights into biological cells with diameters from 1 to 100 μm (Ref. 7) or even the determination of impurities and intoxicants enriched inside them. Further improvement will enable the observation of genetic information (DNA).^{8–10}

According to Abbe's diffraction limit, the minimum spatial resolution for microscopy techniques at a given wavelength λ is $\approx \frac{\lambda}{2}$. For THz radiation, this yields a few hundred micrometers. The simplest approach to overcome this limitation is near-field imaging.^{11–13} For this purpose, the light source spot needs to be limited by an aperture. Simultaneously, the THz generation spot needs to be in the direct vicinity of the investigated structure. Both aperture and distance to the imaged pattern must be much smaller than the generated wavelength. In principle, the dimensions of these two factors limit the possible resolution. Several studies have already demonstrated the huge potential for THz near-field imaging by investigating optical near-fields close to metallic structures. This includes small apertures^{14–18} or microresonators and metamaterials.^{19,20} In those investigations, THz pulses with

large beam dimensions are generated in the far-field and propagate through apertures with subwavelength dimensions to achieve reduced beam diameters. The diffracted waves need to be detected behind those apertures at distances smaller than the wavelengths before diffraction effects occur.^{21–25} Aside from this, there is development in near-field imaging by illuminating whole arrays and reconstructing the images by calculating the signal correlation.²⁶ In this regard, spintronic THz emitters exhibit several possibilities for implementation with biological samples in combination with near-field imaging. They are low-cost, and mass-production is possible by depositing the bilayer heterostructures on a huge variety of glass substrates.

In this study, we investigate spintronic THz emitters, which can be placed in direct proximity to the imaged structure. Femtosecond laser pulses focused down to a few micrometers locally generate THz radiation, confining the spatial expansion of the THz source spot to those dimensions. The specially designed and lithographically prepared test structure consists of an adjacent patterned gold film, separated from the emitter by an insulating spacer layer. THz pulse generation in the direct vicinity of the imaged object generally leads to detection independent of near-field effects, because imaging itself is not affected by diffraction effects. The sample is moved systematically in the x- and y-directions. The THz pulse is generated at each position and images the gold pattern. The results confirm a high near-field spatial resolution of $4.9 \pm 0.4 \mu\text{m}$ for the frequency of 1 THz, which is in the range of the laser spot size. With this approach, the capability for near-field imaging at high spatial resolutions overcomes the Abbe limit by 30 times.^{27–29}

The schematic of the optical setup used for near-field THz imaging is shown in Fig. 1(a). A Ti:Sa laser (Coherent Vitara) with 40 fs

pulse duration at 810 nm central wavelength and a repetition rate of 80 MHz is used as an optical light source for THz pulse generation and stroboscopic detection. The laser beam is split into a pump (solid line) and a probe beam (dashed line). The intense pump beam is guided to the emitter to generate THz radiation. The probe beam is directed through an adjustable temporal delay, enabling a systematic THz pulse sampling in the detection scheme. The THz emitter is a spintronic heterostructure consisting of a ferromagnetic FM and a heavy metal non-magnetic layer NM.^{30–32} Upon laser excitation with a fluence of $3 \pm 1 \text{ mJ}/\text{cm}^2$, electrons in the FM layer are excited and propagated toward the NM layer (z-direction). The majority electrons experience less scattering than the minority electrons and, thus, have longer lifetimes in the excited state.³³ This ensures, a spin-polarized current \mathbf{J}_s arriving in the NM layer. The high spin polarization leads to a motion deflection perpendicular to the propagation direction caused by the inverse spin-hall-effect (ISHE) of the electrons in the NM layer.^{30,34–36} By exchanging energy with the lattice, the electrons relax back to their original positions. The process induces a charge current pulse $\mathbf{J}_C = \Phi_{\text{SH}} \mathbf{J}_s \times \frac{\mathbf{M}}{|\mathbf{M}|}$, where Φ_{SH} is the spin-Hall angle, and \mathbf{M} is the magnetization. As depicted in Fig. 1(b), \mathbf{J}_C flows in the y-direction and occurs on the picosecond time scale corresponding to a Hertzian dipole emitting in the THz frequency range in the z-direction. This method to generate THz radiation is meanwhile well established in various applications.^{37–41}

An Auston switch [photo-conductive antenna (PCA)] is placed 1.4 mm from the emitter and serves as a detector for THz-radiation. The femtosecond laser pulse excites electrons in the PCA gap shorting it. The THz pulse electric field arriving at the gap sets a potential for the excited electrons generating a current and, thus, the detection signal. The current direction is set by the electric field oscillation.

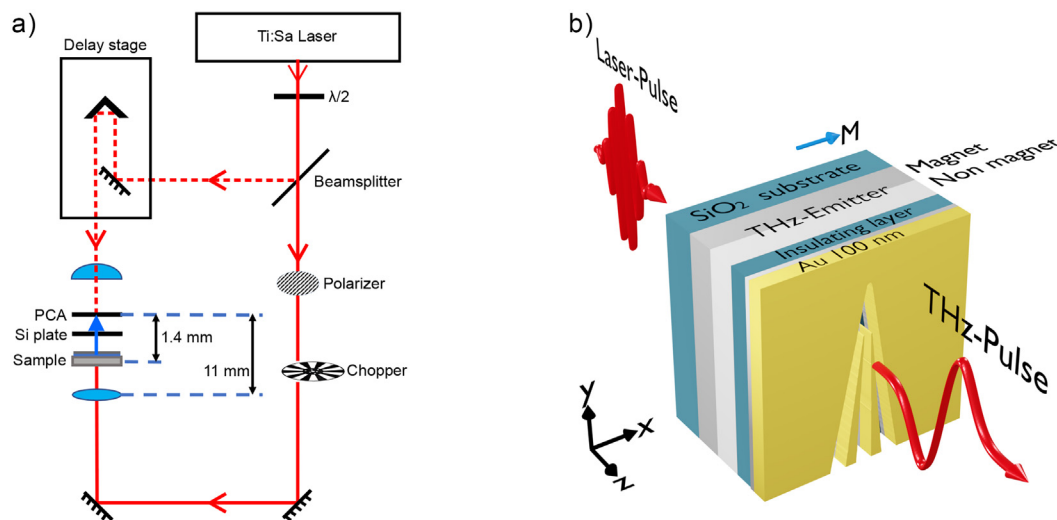


FIG. 1. (a) Scheme of the optical setup. A Ti:sapphire laser system (central wavelength 810 nm, repetition rate 80 MHz, and pulse duration 40 fs) is used as a femtosecond optical source. The laser beam is split into two parts by a beam splitter, a pump (solid line), and a probe (dashed line) beam. The former is guided to the spintronic THz-emitter (sample). The lens in front of the sample confines the pump beam to the micrometer range. The latter is guided through a delay stage for temporal pulse synchronization and focused onto the backside of the detector [photoconductive antenna (PCA)]. At zero delay, the probe pulse excites free charge carriers in the PCA, and the THz-pulse generates an electric field. The resulting electric current in the PCA yields the measurement signal, which is recorded by a lock-in amplifier modulated by a chopper at 1.5 kHz. (b) Schematic of the sample with the THz-emitter heterostructure. A spin current is generated upon femtosecond laser pulse excitation in the ferromagnetic layer (FM) and converted into a transient charge current in the non-magnetic layer (NM) by the inverse spin Hall effect (ISHE), leading to THz emission.

For spin polarization enhancement, we apply a saturating magnetic field $\mu_0 H \approx 10$ mT along the sample plane. The THz E-field amplitude oscillates perpendicular to the magnetic field.³⁰ The 2D scanning capability is implemented by two motorized μm -stages, moving the sample horizontally and vertically in the x- and y-directions with a minimum step size of 200 nm perpendicular to the laser and the THz beam propagation in the z-direction. The frequencies contained in the measured THz pulses are extracted using fast Fourier transformation (FFT).⁴²

As schematically depicted in Fig. 1(b), the sample used to study THz near-field imaging consists of two different units fabricated in two steps. The first unit is a spintronic emitter [Co40Fe40B20 (2 nm)/Pt (2 nm)]. The second unit is a Cr (5 nm)/Au (100 nm) test pattern layer for imaging and resolution determination. A SiO₂ (300 nm) spacer layer, which is much thinner than the THz wavelengths, separates both units. This layout ensures near-field imaging and, at the same time, electric insulation between the emitter and the Au layer. In this construction, a constant distance between both units throughout

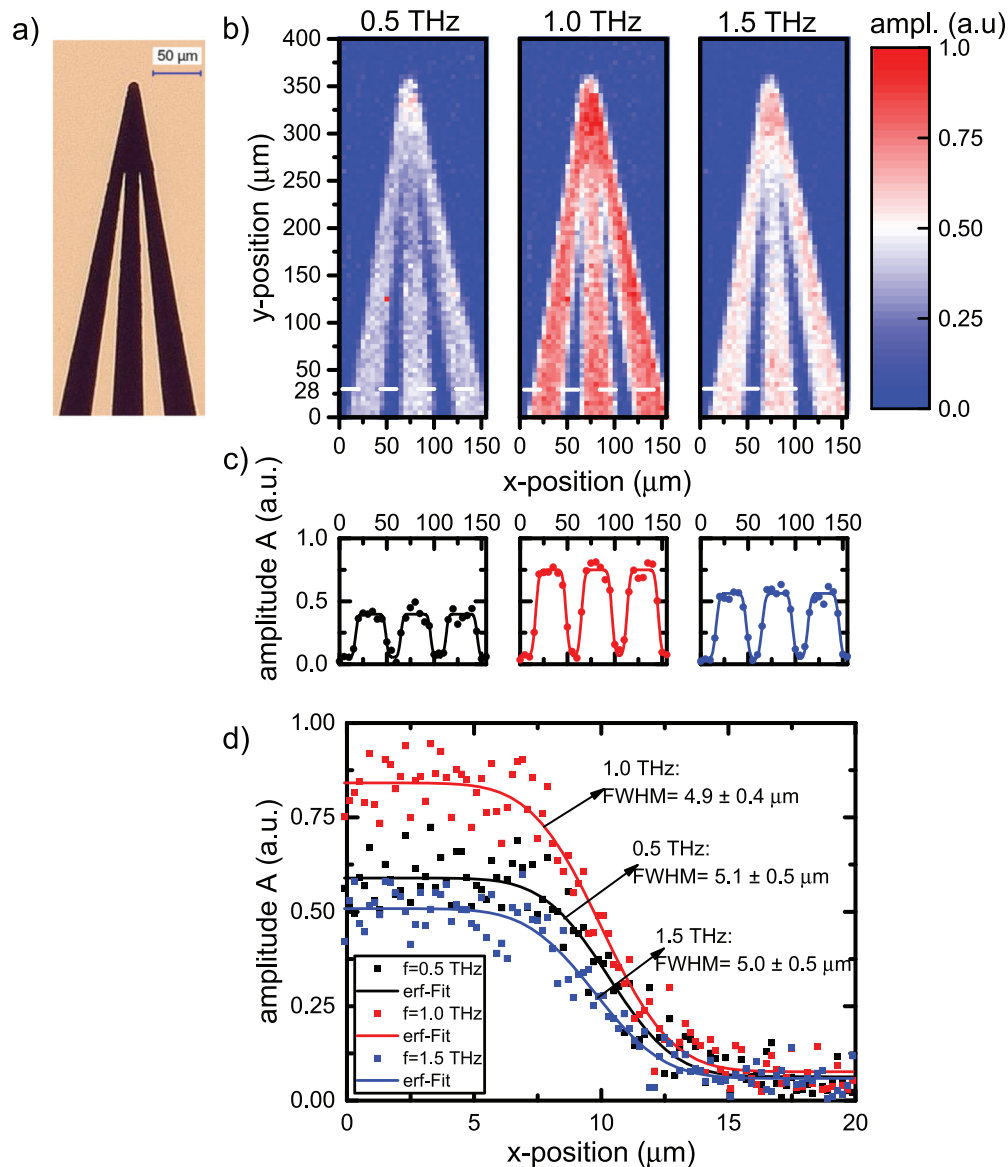


FIG. 2. (a) Optical microscopic image of the designed aperture pattern. (b) Two-dimensional images extracted from near-field THz scanning measurements for 0.5, 1.0, and 1.5 THz. The white dashed lines indicate the position of the intensity profiles shown in (c). The error function fits (lines) to the extracted data (dots) determine the beam dimensions on the order of $5 \mu\text{m}$. (d) Additional small step size $s_{xy} = 0.2 \mu\text{m}$ data for precise resolution determination. The error function fits (erf-fit, lines) to the amplitude profiles determine the full-width half-maximum (FWHM) in the plane of the gold structure on the sample for selected THz frequencies, as indicated by the arrows. Errors to the data points are included in Fig. S3 of the [supplementary material](#).

the sample provides the necessary condition for identical THz pulse generation, ensuring a uniform propagation distance at each position. We fabricate the first unit by depositing the CoFeB layer via magnetron sputtering to establish a homogeneously smooth interface with the subsequently e-beam evaporated heavy metal Pt layer. Within this preparation step, we also deposit the SiO₂ layer by e-beam evaporation to establish equidistant separation of both units. The imaging pattern is created lithographically in the second preparation step and subsequent deposition of the Cr and Au layers, where Cr serves as an adhesive layer for Au.

Figure 2(a) depicts a light microscopic image of the test pattern deposited in direct vicinity to the spintronic emitter layer. The golden area is the layer blocking THz radiation, whereas the three brown slits ensure full THz transmission. This triangular interdigital pattern allows one to adjust the slot size continuously up to ~50 μm width.

Figure 2(b) displays two-dimensional THz images of the test pattern in scale with Fig. 2(a) for three extracted THz frequencies obtained by scanning the sample in x- and y-directions with a step size $s_{xy} = 5 \mu\text{m}$. At each xy-position, a temporal spectrum of the THz pulse with a bandwidth of around 2 THz is recorded. The included frequencies are extracted from each spectrum by FFT. We show single amplitudes A for the three frequencies 0.5, 1, and 1.5 THz. At 1 THz (red), A has a maximum and decreases to about one half for 0.5 and 1.5 THz (both white). The data evaluation process is outlined in the supplementary material, showing the measured THz pulse in Fig. S1 and the frequency spectrum in Fig. S2. The measurements with the PCA detectors yield a bandwidth of 0.4 to 2 THz. For all three THz frequencies, the slit structure is clearly imaged with the Au layer completely blocking all THz radiation (blue).

In the next step, the resolution is determined using the Rayleigh criterion. According to this, for Airy disk shape light distribution, it is possible to distinguish between two equal point sources if they are separated by a distance equal to the length between the center and the first minimum. That means, the maximum of the second point source must be located in the minimum of the first Airy disk. In this case, the amplitude in the overlap region drops down to 73.5% of both sources maximum amplitude providing a contrast of 15% and, thus, discriminability.⁴³ In another view, the full-width half-maximum (FWHM) diameter of the light source determines the lower limit for the resolution. In our approach, the emitted THz pulses have a Gaussian amplitude distribution around the propagation axis, originating from the shape of the exciting laser beam. Therefore, the FWHM diameter of the emitted THz waves in the near-field limit determines the possible resolution. In Fig. 2(c), the amplitudes extracted at the cross section along the white lines in Fig. 2(b) show multiple transitions between the THz radiation blocking and transmitting areas. This corresponds to knife-edge measurements, which are a valid method to determine the spot size.^{44–46} Their transition widths are determined by fitting error functions (lines) to the experimental data (dots), providing the FWHM diameter of the THz beams. The exact used function is $A = \frac{A_0}{2} \cdot \text{erf}\left(\sqrt{2\ln(4)} \cdot \frac{x+x_0}{\text{FWHM}} + A_{\text{off}}\right)$, where A_0 is the amplitude difference between the transmitted and blocked THz signal, x_0 is the slit position offset, and A_{off} takes the background noise into account. The extracted FWHM values are for the 0.5 THz beam $5.9 \pm 1.3 \mu\text{m}$, for the 1.0 THz beam $6.1 \pm 1.0 \mu\text{m}$, and for the 1.5 THz beam $5.8 \pm 1.1 \mu\text{m}$. To ensure, to which extend the step size ($s_{xy} = 5 \mu\text{m}$)

limits the resolution rather than the spot size, Fig. 2(d) shows additional measurements with a reduced step size $s_{xy} = 0.2 \mu\text{m}$. The amplitude data are plotted (dots) together with the corresponding function fits (solid lines) for 1 (red), 0.5 (black), and 1.5 THz (blue). The FWHM in the plane of the Au layer determined for 1.0 THz is $4.9 \pm 0.4 \mu\text{m}$, for 0.5 THz is $5.1 \pm 0.5 \mu\text{m}$, and for 1.5 THz is $5.0 \pm 0.5 \mu\text{m}$. The supplementary material shows details on the error discussion in Fig. S3. The determined resolution for this frequency range is the same within the given error. The expected resolution limit for imaging in the far-field is in the range from 100 to 300 μm for radiation from 1 to 3 THz. Here, the application of the near-field imaging technique improves the resolution by a factor of 20–60.

To support the experimental approach, the spatial THz beam broadening due to divergence during propagation in the intermediate distance between the THz generator and the imaged structure and its propagation toward the detector are investigated by simulation. For this purpose, we divide the distance between the emitter and the detector into two parts $d = d_1 + d_2$. In the first part, we study the beam expansion on the $d_1 = 300 \text{ nm}$ path through the SiO₂ spacer layer, corresponding to the z-direction in the experiment. In the second part, we investigate the distance between the test structure and the detector for three distances, $d_2 = 500 \text{ nm}$, 300 μm, and 2 mm. For the wave propagation through the SiO₂ spacer layer, the wave equation derived from Maxwell equations is solved for a wave package with 1 THz central frequency. In this simulation, the time is iterated from $t = 0 \text{ ps}$ in steps of $\Delta t = 10 \text{ ps}$ up to $t = 2 \text{ ps}$ after generation,

$$\frac{\partial^2 \vec{E}}{\partial t^2} = c^2 \nabla^2 \vec{E}.$$

Here, \vec{E} is the THz beam electric field amplitude, $c = \frac{c_0}{n}$ is the phase velocity of light considering the medium refractive index n , and ∇ denotes the spatial wave propagation. The used parameters are a THz

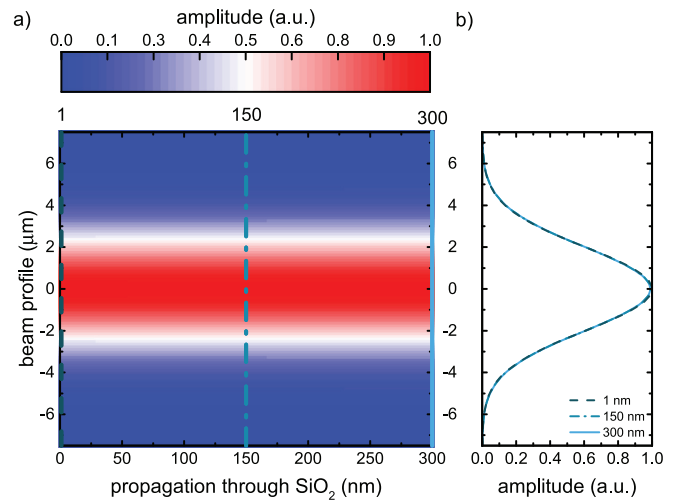


FIG. 3. Simulation of the THz beam propagating distance d_1 through the 300 nm thick SiO₂ layer. (a) Snapshot of the THz beam e-field amplitude distribution 1 ps after generation at $d_1 = 0 \text{ nm}$. Starting with a FWHM = 4.7 μm at the point of generation $d_1 = 0 \text{ nm}$, the Gaussian beam diverges insignificantly after propagating the distance $d_1 = 300 \text{ nm}$, as depicted for three extracted profiles in (b). Multimedia view: <https://doi.org/10.1063/5.0076880.1>

pulse with 1 ps duration, a Gaussian beam spot with a FWHM = 4.7 μm , and a refractive index for THz wavelengths in SiO_2 of $n = 2$.^{47,48}

The simulation results show the THz wave propagating through the SiO_2 spacer layer. The snapshot in Fig. 3(a) (Multimedia view) demonstrates the wave package with a central wavelength $\lambda = 300 \mu\text{m}$ at $t = 1 \text{ ps}$ after generation at point $d_1 = 0 \text{ nm}$ (Pt layer) propagating toward $d_1 = 300 \text{ nm}$ (Au layer). Note, only the peak of the wave package is visible within this 300 nm window. The temporal wave package propagation is included in Fig. 3(a). The spatial amplitude distribution broadens insignificantly as extracted for $d_1 = 1 \text{ nm}$, $d_1 = 150 \text{ nm}$, and $d_1 = 300 \text{ nm}$ in Fig. 3(b), indicating a very slight divergency. Gauss fits to the amplitude distributions obtained throughout the

whole time-interval reveal that the initial FWHM increases by around 1% at this distance. This confirms that defocusing happens on larger length scales and the THz beam stays focused within the spacer layer. Further simulations for larger distances show that propagation through spacer thicknesses in the micrometer range lead to a beam width expansion just below 10% for spacer layer materials with a refractive index below $n = 2$.

The second simulation describes the THz-wave package after diffraction at the test pattern as it propagates the distance d_2 to the detector through air. This part of calculation is performed using energy conservation, the Huygens-Fresnel principle, and the superposition principle with complex-phase-corrected addition. The simulation starts with a Gaussian electric field distribution in the test pattern

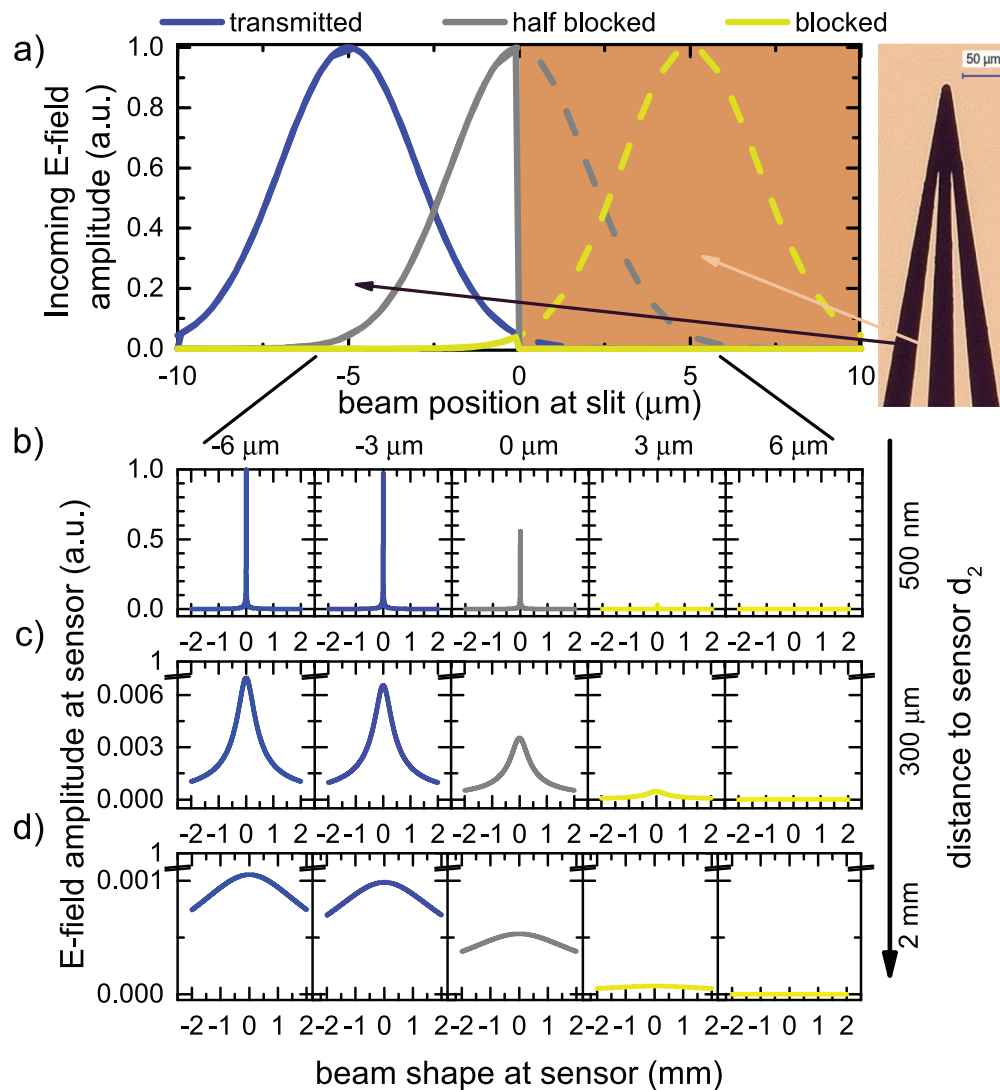


FIG. 4. Intensity calculation for THz waves propagating distance d_2 from the slit to detector through air. (a) Schematic of Gaussian beams at the slit plane. The solid lines represent the parts passing the plane, and the dashed lines the parts blocked by the gold layer (orange). (b)–(d) Calculated E-field amplitudes in the sensor plane for three distances $d_2 = 500 \text{ nm}$, $300 \mu\text{m}$, and 2 mm . The blue colors represent beams fully passing the slit, the gray color the half-blocked beam, and the yellow colors the beams more than half blocked at the slit. The E-field amplitudes at the sensor decrease with the distance d_2 because of the spherical expansion of the THz wave package.

plane and calculates the electric field distribution arriving in the detector plane placed at d_2 . The electric fields are normed to the amplitude in the test pattern plane at $d_1 = 300$ nm from the emitter after the propagation distance through SiO₂. The computed results are presented in Fig. 4 and additionally summed up in Fig. 5 (Multimedia view).

Figure 4(a) illustrates the Gaussian beam at the test pattern plane. The region with negative beam positions at the slit is fully transmitting (white) and with positive positions fully blocking the beam (orange). The knife-edge is located at position = 0 μ m. Beam spots with a Gaussian electric field amplitude distribution whose center is in the transmitting region are fully or partially transmitted, represented in blue, whereas beam spots, whose center is located in the blocking region, are partially or fully blocked represented in yellow. Simulation starts with a Gaussian beam with a FWHM = 4.7 μ m and calculates the beam shape at the sensor for beam positions at the slit ranging from -10 to $+10$ μ m. The resulting THz beam e-field amplitudes arriving at the sensor for three sensor distances ($d_2 = 500$ nm, 300 μ m, 2 mm) are depicted in Figs. 4(b)–4(d), respectively. The electric field amplitudes arriving at the sensor are shown in blue, gray, and yellow colors corresponding to Fig. 4(a). At the first sensor distance,

$d_2 = 500$ nm behind the test pattern, shown in Fig. 4(b), only a small expansion occurs, and the peak electric field amplitude is in the range of the incoming wave. For larger detector distances on the order of the wavelength $d_2 = 300$ μ m, the THz e-field distribution diverges into the millimeter scale [see Fig. 4(c)], and even further for $d_2 = 2$ mm shown in Fig. 4(d). At the same time, the THz peak electric field amplitude decreases with the sensor distance $\sim 1/d_2$, as expected for spherical waves. Moreover, the amplitudes on the sensor decrease, when the beam is moved from the transmitting to blocking region across the knife-edge. In Figs. 4(b)–4(d), this decrease is visible as a function of the beam position at the slit and returns the FWHM = 4.7 μ m of the starting beam.

Both simulation results support the experimental data, showing that the resolution of THz imaging with wavelengths $\lambda > 100$ μ m in the near-field approach can be enhanced to the micrometer range, limited only by the optical properties of the excitation light waves. Therefore, by using objectives for the pump laser beam, a resolution even below the micrometer scale will be possible. Aside from this, simulations show very homogeneous and almost spherical wave propagation, which means there are no interference minima that need to be avoided while adjusting the detector. Furthermore, two parameters are

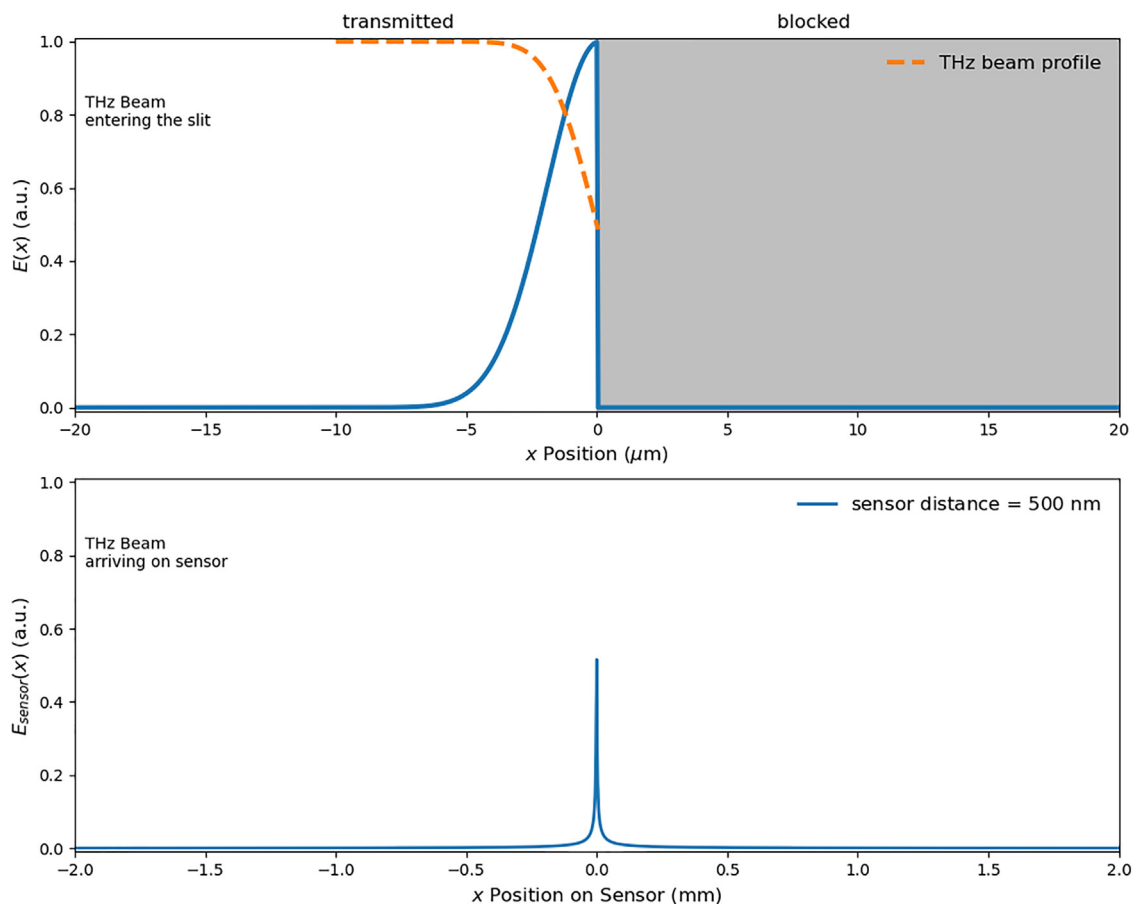


FIG. 5. Representation of the simulation results discussed in Fig. 4 and presented as multimedia movie. The top panel shows the incoming beam profile passing the slit. The lower panel shows the beam amplitude arriving at the sensor for three different sensor distances d_2 . Multimedia view: <https://doi.org/10.1063/5.0076880.2>

revealed whose control will lead to a significant gain of the measurement signal. First, the intensity of the THz wave propagating to the detector decreases by $\sim 1/d_2$ with the detector distance. This requires detector positioning within a vicinity of a few millimeters behind the emitter. Second, the intensity distribution diverges significantly due to the strong focusing of the exciting light beam for THz wave generation. Therefore, implementing microlenses that are collimating directly into the plane of the imaged pattern would improve the signal. Lenses with such dimensions can be produced using three-dimensional lithography techniques directly on top of the emitters.

The results of our study clearly demonstrate the potential for near-field THz imaging using spintronic heterostructure-based emitters. Their resolution can be enhanced below $1\ \mu\text{m}$, and the emitter heterostructures can be deposited directly on glass surfaces, e.g., microscope slides or coverslips. The distance between the emitter and the imaged objects can be kept constant by adding nanometer-thick spacer layers. This layout ensures identical conditions for THz wave generation on each spot and offers ideal conditions for imaging using the two-dimensional scanning technique. Our near-field imaging approach will enable the investigation of biological cells or blood platelets using THz radiation. In the future, more data revealing the spectral absorption of polymers in this range will make this technique available for investigations of plastic nanoparticle residues in human cells. Also, insights into the specifics of spectral absorption will allow distinguishing between cell types and enable the identification of cancer cells or blood platelet malformations. Moreover, this technique still offers signal-to-noise ratio improvement by implementing collimating nanolenses to avoid beam divergence after transmission through the imaged objects. This will not only increase the signal intensity on the detector but also permit for more flexible detector positioning at larger distances to the samples. In addition, the implementation of a newer generation of PCA detectors⁴⁹ or other detection techniques, like electro-optic detection with ZnTe crystals,³¹ will expand the investigated spectral range.

See the [supplementary material](#) for details regarding the data evaluation, showing one example THz spectrum and its frequency spectrum obtained via FFT and the error and residual data from the resolution measurements in [Fig. 2\(d\)](#).

The authors gratefully acknowledge the financial support from the BMBF, MetaZIK PlasMark-T (No. FKZ:03Z22C511). Y.S. acknowledges the Graduate Program in Spintronics (GP-Spin) at Tohoku University.

AUTHOR DECLARATIONS

Conflict of Interest

The authors have no conflicts of interest to disclose.

DATA AVAILABILITY

The data that support the findings of this study are available from the corresponding author upon reasonable request.

REFERENCES

- A. Y. Pawar, D. D. Sonawane, K. B. Erande, and D. V. Derle, *Drug Invent. Today* **5**, 157 (2013).
- P. H. Siegel, *IEEE Trans. Microwave Theory Tech.* **52**, 2438 (2004).
- H. Cheon, J. H. Paik, M. Choi, H.-J. Yang, and J.-H. Son, *Sci. Rep.* **9**, 6413 (2019).
- A. J. Fitzgerald, E. Berry, N. N. Zinovev, G. C. Walker, M. A. Smith, and J. M. Chamberlain, *Phys. Med. Biol.* **47**, R67 (2002).
- R. E. Allman and R. J. Foltynowicz, "Terahertz time-domain spectroscopy of atmospheric water vapor from 0.4 to 2.7 THz," Technical Report No. SAND2005-5709 (Sandia National Laboratories, 2005).
- D. M. Slocum, E. J. Slingerland, R. H. Giles, and T. M. Goyette, *J. Quant. Spectrosc. Radiat. Transfer* **127**, 49 (2013).
- G. Bao and S. Suresh, *Nat. Mater.* **2**, 715 (2003).
- A. Veeraselvam, G. N. A. Mohammed, K. Savarimuthu, and R. Sankararajan, *Opt. Quantum Electron.* **53**, 354 (2021).
- X. Yang, X. Zhao, K. Yang, Y. Liu, Y. Liu, W. Fu, and Y. Luo, *Trends Biotechnol.* **34**, 810 (2016).
- Y. Peng, C. Shi, X. Wu, Y. Zhu, and S. Zhuang, *BME Front.* **2020**, 1–11.
- E. Betzig and J. K. Trautman, *Science* **257**, 189 (1992).
- S. Hunsche, M. Koch, I. Brener, and M. C. Nuss, *Opt. Commun.* **150**, 22 (1998).
- Z. Jiang, X. G. Xu, and X.-C. Zhang, *Appl. Opt.* **39**, 2982 (2000).
- O. Mitrofanov, M. Lee, J. W. Hsu, L. N. Pfeiffer, K. W. West, J. D. Wynn, and J. F. Federici, *Appl. Phys. Lett.* **79**, 907 (2001).
- A. Bitzer and M. Walther, *Appl. Phys. Lett.* **92**, 231101 (2008).
- A. J. Adam, J. M. Brok, M. A. Seo, K. J. Ahn, D. S. Kim, J. H. Kang, Q. H. Park, M. Nagel, and P. C. Planken, *Opt. Express* **16**, 7407 (2008).
- L. Guestin, A. J. Adam, J. R. Knab, M. Nagel, and P. C. Planken, *Opt. Express* **17**, 17412 (2009).
- J. R. Knab, A. J. Adam, M. Nagel, E. Shaner, M. A. Seo, D. S. Kim, and P. C. Planken, *Opt. Express* **17**, 15072 (2009).
- D. W. Vogt, A. H. Jones, T. A. Haase, and R. Leonhardt, *Photonics Res.* **8**, 1183 (2020).
- N. Sulollari, J. Keeley, S. Park, P. Rubino, A. D. Burnett, L. Li, M. C. Rosamond, E. H. Linfield, A. G. Davies, J. E. Cunningham, and P. Dean, *APL Photonics* **6**, 066104 (2021).
- Q. Chen, Z. Jiang, G. X. Xu, and X.-C. Zhang, *Opt. Lett.* **25**, 1122 (2000).
- H.-T. Chen, R. Kersting, and G. C. Cho, *Appl. Phys. Lett.* **83**, 3009 (2003).
- A. J. Huber, F. Keilmann, J. Wittborn, J. Aizpurua, and R. Hillenbrand, *Nano Lett.* **8**, 3766 (2008).
- F. Blanchard, A. Doi, T. Tanaka, H. Hirori, H. Tanaka, Y. Kadoya, and K. Tanaka, *Opt. Express* **19**, 8277 (2011).
- M. Baillergeau, K. Maussang, T. Nirrengarten, J. Palomo, L. H. Li, E. H. Linfield, A. G. Davies, S. Dhillon, J. Tignon, and J. Mangeney, *Sci. Rep.* **6**, 24811 (2016).
- S.-C. Chen, Z. Feng, J. Li, W. Tan, L.-H. Du, J. Cai, Y. Ma, K. He, H. Ding, Z.-H. Zhai, Z.-R. Li, C.-W. Qiu, X.-C. Zhang, and L.-G. Zhu, *Light* **9**, 99 (2020).
- G. Acuna, S. F. Heucke, F. Kuchler, H.-T. Chen, A. J. Taylor, and R. Kersting, *Opt. Express* **16**, 18745 (2008).
- A. Bitzer, H. Merbold, A. Thoman, T. Feurer, H. Helm, and M. Walther, *Opt. Express* **17**, 3826 (2009).
- D. Yang, J. Liang, C. Zhou, L. Sun, R. Zheng, S. Luo, Y. Wu, and J. Qi, *Adv. Opt. Mater.* **4**, 1944 (2016).
- T. Kampfrath, M. Battiato, P. Maldonado, G. Eilers, J. Nötzold, S. Mährlein, V. Zbarsky, F. Freimuth, Y. Mokrousov, S. Blügel, M. Wolf, I. Radu, P. M. Oppeneer, and M. Münzenberg, *Nat. Nanotechnol.* **8**, 256 (2013).
- T. Seifert, S. Jaiswal, U. Martens, J. Hannegan, L. Braun, P. Maldonado, F. Freimuth, A. Kronenberg, J. Henrizi, I. Radu *et al.*, *Nat. Photonics* **10**, 483 (2016).
- Y. Wu, M. Elyasi, X. Qiu, M. Chen, Y. Liu, L. Ke, and H. Yang, *Adv. Mater.* **29**, 1603031 (2017).
- M. Battiato, K. Carva, and P. M. Oppeneer, *Phys. Rev. Lett.* **105**, 27203 (2010).
- E. Saitoh, M. Ueda, H. Miyajima, and G. Tataru, *Appl. Phys. Lett.* **88**, 182509 (2006).
- D. Wei, M. Obstbaum, M. Ribow, C. H. Back, and G. Woltersdorf, *Nat. Commun.* **5**, 3768 (2014).
- J. Sinova, S. O. Valenzuela, J. Wunderlich, C. H. Back, and T. Jungwirth, *Rev. Mod. Phys.* **87**, 1213 (2015).
- T. Seifert, S. Jaiswal, M. Sajadi, G. Jakob, S. Winnerl, M. Wolf, M. Kläui, and T. Kampfrath, *Appl. Phys. Lett.* **110**, 252402 (2017).

- ³⁸Z. Jin, A. Tkach, F. Casper, V. Spetter, H. Grimm, A. Thomas, T. Kampfrath, M. Bonn, M. Kläui, and D. Turchinovich, *Nat. Phys.* **11**, 761 (2015).
- ³⁹E. T. Papaioannou, G. Torosyan, S. Keller, L. Scheuer, M. Battiato, V. K. Mag-Usara, J. L'huillier, M. Tani, and R. Beigang, *IEEE Trans. Magn.* **54**, 9100205 (2018).
- ⁴⁰E. T. Papaioannou and R. Beigang, *Nanophotonics* **10**, 1243 (2020).
- ⁴¹Y. Sasaki, K. Z. Suzuki, and S. Mizukami, *Appl. Phys. Lett.* **111**, 102401 (2017).
- ⁴²J. W. Cooley and J. W. Tukey, *Math. Comput.* **19**, 297 (1965).
- ⁴³G. Cox, *Optical Imaging Techniques in Cell Biology* (CRC Press, 2006).
- ⁴⁴W. Plass, R. Maestle, K. Wittig, A. Voss, and A. Giesen, *Opt. Commun.* **134**, 21 (1997).
- ⁴⁵L. Bachmann, D. Maria Zezell, and E. Puig Maldonado, *Instrum. Sci. Technol.* **31**, 47 (2003).
- ⁴⁶G. Ok, S.-W. Choi, K. H. Park, and H. S. Chun, *Sensors* **13**, 71 (2012).
- ⁴⁷T. Henning and H. Mutschke, *Low-Temperature Infrared Properties of Cosmic Dust Analogues*, 327th ed. (Astronomy and Astrophysics, 1997).
- ⁴⁸R. Kitamura, L. Pilon, and M. Jonasz, *Appl. Opt.* **46**, 8118 (2007).
- ⁴⁹J. Neu and C. A. Schmuttenmaer, *J. Appl. Phys.* **124**, 231101 (2018).